Journal of Nuclear Materials 407 (2010) 88–99

Contents lists available at ScienceDirect

Journal of Nuclear Materials

journal homepage: www.elsevier.com/locate/jnucmat

Structural characterization of Nd-doped Hf-zirconolite $Ca_{1-x}Nd_xHfTi_{2-x}Al_xO_7$ ceramics

Daniel Caurant *, Pascal Loiseau, Isabelle Bardez [1]

Laboratoire de Chimie de la Matière Condensée de Paris (UMR-CNRS 7574), Chimie-ParisTech (ENSCP), 11 rue Pierre et Marie Curie, 75231 Paris, France

ARTICLE INFO

Article history:
Received 28 June 2010
Accepted 22 September 2010

ABSTRACT

Because of its high incorporation capacity and of the high thermal neutron capture cross-section of hafnium, Hf-zirconolite ($CaHfTi_2O_7$) ceramic can be envisaged as a potential waste form for minor actinides (Np, Am, Cm) and plutonium immobilization. In this work, Nd-doped Hf-zirconolite $Ca_{1-x}Nd_xHfTi_{2-x}Al_xO_7$ ($x = 0$; 0.01 and 0.2) ceramics have been prepared by solid state reaction. Neodymium has been used as trivalent actinide surrogate. The ceramic samples structure has been studied by X-ray diffraction and refined by the Rietveld method. This revealed that Nd^{3+} ions only enter the Ca site, whereas part of Hf^{4+} ions substitute titanium into Ti(1) sites and Al^{3+} ions mainly occupy the Ti(2) split sites and Ti(3) sites of the zirconolite structure. Using various spectroscopic techniques (electron spin resonance, optical absorption and fluorescence), the environment of Nd^{3+} cations in Hf-zirconolite has been studied and compared with that of Nd^{3+} cations in Zr-zirconolite ($CaZrTi_2O_7$). Different local environments of Nd^{3+} cations have been detected in Hf-zirconolite that can be attributed to the existence of an important disorder around Nd in the Ca site probably due to the statistical occupancy of the next nearest cationic site of neodymium (a split Ti site) by Ti^{4+}, Al^{3+} cations and vacancies. No significant differences were observed concerning Nd^{3+} cations environment and distribution in Hf- and Zr-zirconolite ceramics.

1. Introduction

Due to the main contribution of minor actinides (Np, Am, Cm) to the long term radiotoxicity of high-level nuclear wastes (HLW) recovered after spent fuel reprocessing, researches have been led in several countries – such as in France [1,2], in Japan and in Russia [3] – on the enhanced separation of minor actinides from nuclear spent fuel and on their incorporation in highly durable matrices (ceramics, glass–ceramics or glasses) [3–15]. Moreover, studies on waste forms – mainly single phase ceramics – for plutonium disposition have also been performed in USA and Russia [6,12,16] to immobilize excess weapons plutonium whereas other studies are in progress in United Kingdom on the immobilization of waste PuO_2 unsuitable for mixed oxide fuel fabrication [17–20].

Zr-zirconolite (nominally $CaZrTi_2O_7$) is one of the best single phase ceramic that has been proposed and retained as a host phase for the immobilization of separated minor actinides by considering all its performances (waste loading, aqueous durability, chemical flexibility, radiation resistance, existence of natural analogues) [4,7,8,21–24]. Moreover, this phase is considered as one of the best ceramic waste form candidate for the immobilization of waste PuO_2 in United Kingdom [18,20] and in United States [25]. Zr-zirconolite was initially envisaged in the SYNROC waste forms developed in Australia which is an assemblage of three main thermodynamically compatible titanate crystalline phases (zirconolite + perovskite + hollandite) adapted for the immobilization of non separated HLW (fission products + minor actinides) [26,27]. Zirconolite-based titanate ceramics containing about 80–90% zirconolite and 10–20% Ba-hollandite + rutile have been also recently envisaged for the immobilization of impure plutonium or separated actinide-rich wastes [28]. In this case, Ba-hollandite would be present in the waste forms to provide a host phase for radioactive cesium and would act here as an internal radiation barrier to prevent the diversion risks of plutonium.

Despite its tendency to amorphization under the alpha decay damages both in very old natural samples (containing U and Th) [29–32] and in artificial ceramics (containing ^{244}Cm or ^{238}Pu for instance) [25,33], Zr-zirconolite keeps its very high chemical durability which is mainly due to the occurrence of high amounts of both TiO_2 and ZrO_2 in its composition. The small effect of alpha decay on the chemical durability of Zr-zirconolite was also confirmed both after external irradiation experiments with heavy ions simulating alpha-recoils and by studying natural zirconolite metamict samples [8,34]. Studies have also been recently performed on helium release from ^{244}Cm, ^{238}Pu and ^{239}Pu doped Zr-zirconolite ceramics [35].

* Corresponding author. Tel.: +33 153767922; fax: +33 146347489.
E-mail address: daniel-caurant@chimie-paristech.fr (D. Caurant).
[1] Present address: Commissariat à l'Energie Atomique (CEA) Valrho, Marcoule, 30207 Bagnols-sur-Cèze, France.

0022-3115/$ - see front matter © 2010 Elsevier B.V. All rights reserved.
doi:10.1016/j.jnucmat.2010.09.033

The structure of Zr-zirconolite is monoclinic ($C_{2/c}$ space group for the polytype-2M) [36,37] and can be described by the stacking along c of two modules (Fig. 1a). Each module is constituted of two successive (0 0 1) layers: the first one consists of alternate row of CaO_8 and ZrO_7 polyhedra, whereas the second one contains TiO_6 polyhedra (corresponding to Ti(1) and Ti(3) sites). These last layers also contains TiO_5 polyhedra corresponding to the statistic occupancy of the split titanium sites (Ti(2)) [38]. In zirconolite, the actinides and their surrogates (lanthanides) incorporated either into the Ca or Zr sites of the structure (Fig. 1) [39–45]. Because of their similar charge and close ionic radii [46], Nd^{3+} cation is generally considered as a good surrogate for Am^{3+} and Cm^{3+} cations and is used to prepare waste form samples in laboratories that cannot manipulate radioactive materials. It was shown that more than 60% of the Ca^{2+} cations of Zr-zirconolite could be replaced by Nd^{3+} or Gd^{3+} cations without changing the structure, following a charge compensation scheme with Al^{3+} cations into the titanium sites according to the following formula $Ca_{1-x}Nd_xZrTi_{2-x}Al_xO_7$ [47–49]. Moreover, we showed, using structure refinement by the Rielveld method for the $Ca_{0.7}Nd_{0.3}ZrTi_{1.7}Al_{0.3}O_7$ composition (i.e. with $x = 0.3$), that Nd^{3+} cations mainly entered into the calcium site and that Al^{3+} cations entered into the Ti(2) site [4,48]. Similarly, using both Rietveld refinement of X-ray powder data and ^{57}Fe Mössbauer spectroscopy, Lumpkin et al. showed that Fe preferentially occupied the five coordinated Ti(2) site in $CaZrTi_{2-2x}Nb_xFe_xO_7$ zirconolite samples [50]. We also reported that it was possible to prepare lanthanide (Ln)-doped glass–ceramic samples containing only Zr-zirconolite crystals in their bulk after nucleation and crystal growth heat treatments of appropriate parent glasses belonging to the SiO_2–Al_2O_3–CaO–TiO_2–ZrO_2–Ln_2O_3 system [9,10,51–56]. In this case, we showed that minor actinides and Pu surrogates (lanthanides) were partially immobilized in the Ca and Zr sites of zirconolite crystals. More recently, Mahmoudysepehr et al. also prepared Zr-zirconolite based glass–ceramics for radioactive waste immobilization but from less refractory glass compositions belonging to the SiO_2–PbO–CaO–ZrO_2–TiO_2–B_2O_3–K_2O system [57].

As Zr^{4+} and Hf^{4+} cations have nearly identical radii (respectively 0.78 Å and 0.76 Å in sevenfold coordination [46] corresponding to that of Zr and Hf sites in zirconolite, Fig. 1) and belong to the same column of the periodic table, these two elements have very similar chemical properties and are expected to be incorporated in similar crystalline structures. Indeed, this was demonstrated for natural and synthetic Zr-rich crystalline phases such as zircon [30,58,59], baddeleyite [60] and zirconolite. For instance, natural zirconolite samples were shown to incorporate 2.4 wt.% HfO_2 [61]. Moreover, the possibility to prepare (Zr, Hf)-zirconolite $CaZr_{1-x}Hf_xTi_2O_7$ ($0 < x \leqslant 1$) ceramic samples was reported in literature and Hf-zirconolite $CaHfTi_2O_7$ has a structure similar to that of Zr-zirconolite (Fig. 1) [7,47,62–64]. As hafnium has a high thermal neutron capture cross-section in comparison with zirconium (respectively 104 and 0.184 barns [65]), it is considered as a neutron poison for fission reactions. This is why it would be interesting to substitute either totally or partially Zr by Hf in the zirconolite crystals of the ceramics and glass–ceramics to prevent criticality events in waste forms heavily loaded with fissile actinide isotopes such as ^{239}Pu. However, as hafnium is less abundant in earth's crust than zirconium (Hf/Zr = 0.028 in weight [65]), hafnium compounds are more expensive than zirconium ones. Gd which is a very good neutron absorber (thermal neutron capture cross-section = 49,000 barns [65]) can also be incorporated in the Hf-zirconolite-2M structure following for instance the composition $Ca_xGd_{2(1-x)}Hf_xTi_2O_7$ ($x < 0.29$) [66] which is very similar to the case of $Ca_xGd_{2(1-x)}Zr_xTi_2O_7$ for which the polytype-2M was observed up to $x \approx 0.24$ [63,67]. The possibility to incorporate both trivalent and tetravalent plutonium in Hf-zirconolite was also demonstrated

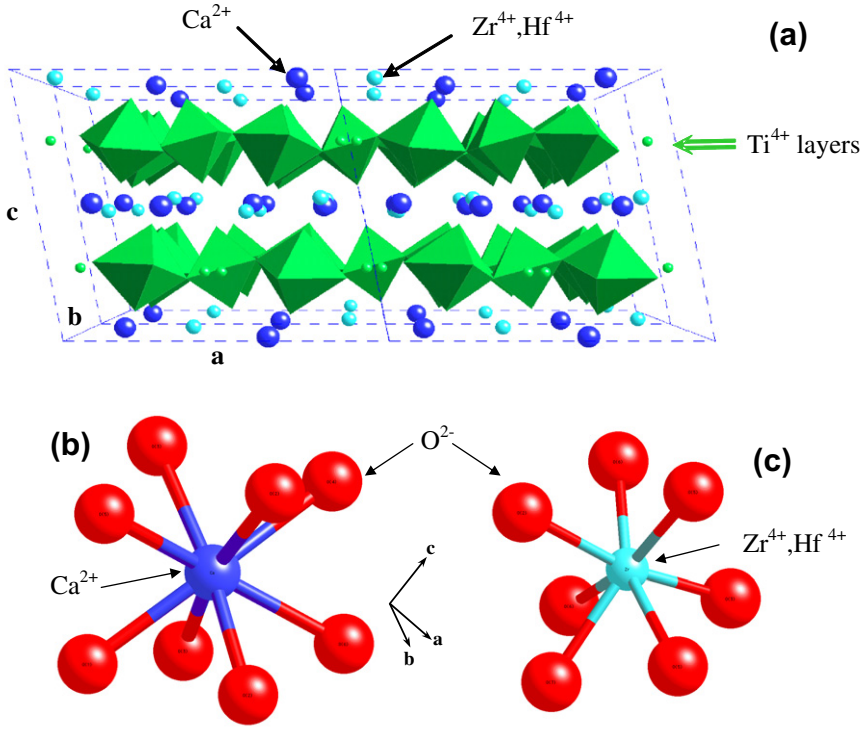

Fig. 1. (a) Hf- and Zr- zirconolite $Ca(Hf, Zr)Ti_2O_7$ structure (monoclinic structure, space group $C_{2/c}$) showing the TiO_6 octahedrons (Ti(1) and Ti(3) sites) layers and the (Ca^{2+}, Hf^{4+}, Zr^{4+}) rows. The polyhedra corresponding to the Ti^{4+} cations in fivefold coordination (Ti(2) site) are not drawn but this splitted site – which is statistically occupied [38] – is shown (small balls in the Ti^{4+} layers). For clarity reasons oxygen atoms are not drawn in the figure. Ca^{2+} cations are located in eightfold coordinated sites (b) whereas Hf^{4+} and Zr^{4+} cations are located in sevenfold coordinated sites (c). The a, b and c directions of the monoclinic cell are shown near the two sites.

[39]. Concerning the chemical durability of zirconolite containing hafnium, several results reported in literature indicated that there is only little difference between the leaching behavior of Hf and Zr [68,69]. To the best of our knowledge, no comparison has been reported in literature on the behavior of Zr- and Hf-zirconolite under internal or external irradiation to simulate α-decay. Nevertheless, external irradiation experiments with heavy ions performed on $La_2Zr_2O_7$ and $La_2Hf_2O_7$ pyrochlore ceramics showed that the substitution of Zr by Hf in the composition might have a significant impact on critical amorphization dose, critical temperature and activation energy for thermal recovery of damage [70]. This was recently confirmed by the study of the resistance to damage by heavy ions irradiation of $Ca_3Zr_2FeAlSiO_{12}$ and $Ca_3Hf_2FeAlSiO_{12}$ ceramics considered as potential host phases for actinide waste immobilization [71].

In previous papers [72,73], we showed that it was possible to prepare Nd-doped (Zr, Hf)-zirconolite-based glass–ceramics from SiO_2–Al_2O_3–CaO–TiO_2–(HfO_2, ZrO_2)–Nd_2O_3 parent glasses with $[ZrO_2]/[HfO_2]$ = 0 or 1 using nucleation + crystal growth heat treatments. In this case, the composition of the zirconolite crystals formed in the bulk of the samples was respectively $Ca_{0.85}Nd_{0.21}Hf_{1.08}Ti_{1.71}Al_{0.18}O_7$ and $Ca_{0.85}Nd_{0.20}Zr_{0.59}Hf_{0.49}Ti_{1.71}Al_{0.16}O_7$ as determined by electron probe microanalysis. It appeared that nearly the same amount of neodymium was incorporated in the crystals (Al^{3+} cations ensuring mainly the charge compensation) as for the corresponding parent glass containing only ZrO_2 [52,55].

In this paper we present the preparation method and the structural characterization of Nd-doped Hf-zirconolite ($Ca_{1-x}Nd_xHfTi_{2-x}Al_xO_7$, x = 0; 0.01 and 0.2) ceramic samples. This work was performed in order to study the effect of the total substitution of Zr by Hf in Nd-doped zirconolite on its structure (by X-ray diffraction and Rietveld refinement) and on the local environment of Nd^{3+} cations by using different spectroscopic methods (optical absorption and fluorescence, electron spin resonance). Comparisons are made with Nd-doped Zr-zirconolite ceramics previously studied by the authors [48,74]. The Hf-zirconolite samples prepared in this work have also been used as reference samples for studies on Nd-doped Hf-zirconolite-based glass–ceramic waste forms [73,75].

2. Experimental procedure

Three Hf-zirconolite ceramic samples ($Ca_{1-x}Nd_xHfTi_{2-x}Al_xO_7$, x = 0; 0.01 and 0.2) were prepared by an oxide-route method by sintering under air as follows:

- Mixing (≈20 g) and pelletizing by uniaxial pressing at 2 t/cm^2 of reagent grade powders ($CaCO_3$, HfO_2, TiO_2, Al_2O_3, Nd_2O_3).
- First sintering stage at 1400 °C for 100 h followed by grinding and peletizing.
- Second sintering stage at 1460 °C for 100 h. This second stage was performed in order to increase samples homogeneity.

For the X-ray diffraction powder (XRD) measurements, the ceramics were ground and sieved through a 20-μm mesh. Diffraction patterns were collected at room temperature on a Panalytical X'Pert Pro apparatus in Bragg–Brentano geometry operating at Cu $K\alpha_1$ wavelength (λ $K\alpha_1$(Cu) = 1.5406 Å), equipped with a front beam Ge(1 1 1) monochromator and a linear PixCell detector. The structure of the x = 0 and x = 0.2 samples was refined by the Rietveld method using the program Fullprof [76]. For this purpose, XRD patterns were recorded between 2θ = 12° and 122° for x = 0, and 2θ = 12° and 108° for x = 0.2, both at intervals of 0.013° for 1483 s by step (cumulated on the 255 channels of the detector).

Polished and carbon coated sections of the ceramics were analyzed by scanning electron microscopy (SEM) and energy dispersive X-ray analysis (EDX). These experiments were performed at 15 kV and 1.8 nA using a Hitachi S2500 microscope equipped with a PGT analyzer. However due to the occurrence of an overlap on EDX spectra between the strongest hafnium M lines (M_1(Hf) = 1645 eV, M_2(Hf) = 1698 eV) and the aluminum $K\alpha_1$ line ($K\alpha_1$(Al) = 1487 eV), it was not possible to determine correctly the composition of the Nd-doped ceramics containing aluminum ($x \neq 0$) using this technique (see Fig. 4 below). Nevertheless, EDX spectra were recorded to study qualitatively the samples and to determine quantitatively the composition of the perovskite minor phase in the x = 0 sample. In order to get quantitative results on the Hf-zirconolite phase, Electron Probe MicroAnalysis (EPMA) was carried out with the help of a Cameca SX50 apparatus (accelerating voltage 15 kV, beam current 15 nA). HfO_2, andradite ($Ca_3Fe_2Si_3O_{12}$), pyrophanite ($MnTiO_3$), $NdPO_4$ and corundum (Al_2O_3) were used as microprobe standards for Hf, Ca, Ti, Nd and Al respectively.

As Nd^{3+} ($4f^3$) cations are paramagnetic and optically active, they can be detected both by electron spin resonance (ESR) and optical spectroscopies (absorption and fluorescence). These spectroscopic techniques give information about the energy differences between the electronic levels of neodymium cations incorporated in the structure. These energy differences (and thus the spectra) are sensitive to the environment of the cation (local structure) in the material and can be used at least qualitatively to identify the different sites occupied by Nd^{3+} cations in the samples. For instance, the Nd^{3+} cation ground state is $^4I_{9/2}$ which splits into five Stark (or Kramers) doublets under the action of a low symmetry crystal field as it is the case for the calcium site in zirconolite (C_1 symmetry, see Fig. 7b below). The energy difference between these doublets depends on the crystal field intensity and symmetry. Due to the possibility of slight changes concerning the nature and the position of the second neighbors of neodymium in the zirconolite structure (see Section 3), the effective number of Nd sites detected by these local spectroscopic techniques can be higher than the number of sites expected by the crystallographic structure that only gives the mean atomic positions in the lattice. Indeed, using the charge compensation scheme $Ca_{1-x}Nd_xHfTi_{2-x}Al_xO_7$ for the preparation of the Nd-doped Hf-zirconolite ceramics, only one kind of neodymium site (the calcium site) is expected.

The ESR experiments were performed at 12 K (the very short spin relaxation time T_1 of neodymium precluding ESR spectra detection at T > 60 K) to investigate the environment of Nd^{3+} cations as well as the possible occurrence of other paramagnetic elements such as Ti^{3+} cations or impurities (such as Fe^{3+} and V^{4+} cations) in the samples. Moreover, as at 12 K only the lowest Stark doublet of the $^4I_{9/2}$ state is populated (see Fig. 7b below), the neodymium ESR spectra can be treated by an Hamiltonian with an effective electronic spin S = 1/2 for their simulation [77]. Spectra were recorded with a microwave power of 20 mW using a Bruker ESP 300e spectrometer operating at X-band ($\nu \approx 9.5$ GHz) and equipped with a TE_{102} rectangular cavity and an Oxford variable temperature accessory. The software Simphonia program from the Bruker Company was used to simulate the neodymium ESR powder spectra and to extract the main components of the corresponding g tensors.

Optical absorption spectra of Nd^{3+} cations were recorded with a Varian Cary 5E double beam spectrometer at low temperature ($T \approx 10$ K) on KBr pellets (≈200 mg) containing 5–10 wt.% Nd-doped zirconolite. In this low temperature range, only the optical transitions from the lowest Stark doublet of the $^4I_{9/2}$ ground state to the excited states are observed. In this work, the $^4I_{9/2} \rightarrow {}^2P_{1/2}$ transition – occurring in the 431–434 nm (23,050–23,200 cm^{-1}) range – was particularly interesting to study because the degeneracy of the $^2P_{1/2}$ state is not removed by the crystal field occurring

around Nd^{3+} cations (see Fig. 7b below). Thus, in these conditions, each kind of neodymium environment is characterized by only one absorption band.

After selective excitation in the $^4I_{9/2} \rightarrow {}^4F_{3/2}$ absorption band occurring in the 876–885 nm (11,300–11,415 cm^{-1}) range using a Ti-sapphire laser pumped by an argon laser, neodymium fluorescence spectra were recorded at $T < 20$ K for the low Nd-doped $Ca_{0.99}Nd_{0.01}HfTi_{1.99}Al_{0.01}O_7$ ceramic. The $x = 0.01$ sample was chosen rather the $x = 0.2$ sample to avoid charge transfer phenomena between Nd^{3+} cations which may occur for higher doping levels. Fluorescence was studied from the lowest Stark level of the $^4F_{3/2}$ state (the only emitting level at low temperature) to the highest Stark level of the $^4I_{9/2}$ state. Moreover, the fluorescence spectrum ($T < 20$ K) of the low Nd-doped sample was also recorded directly after excitation in the $^4I_{9/2} \rightarrow {}^4G_{92}$, $^2K_{13/2}$ region of the absorption spectrum with an argon laser (514.53 nm; 19,436 cm^{-1}) thus reducing site selective excitation (for a higher energy excitation a wider variety of Nd sites are excited). This enables the determination of the mean energy differences between the five Stark levels originating from the $^4I_{9/2}$ state for the different Nd sites. In all cases, fluorescence spectra were recorded with the help of a PbS cell.

3. Results

3.1. XRD, SEM, EDX and EPMA studies

XRD shows that Hf-zirconolite ceramic samples ($Ca_{1-x}Nd_xHfTi_{2-x}Al_xO_7$, $x = 0$; 0.01 and 0.2) are almost single-phase. For instance, the XRD patterns of the $x = 0$ and $x = 0.2$ samples (Fig. 2) indicates that except a low intensity line near $2\theta = 33$–$33.1°$, which proves the existence of a small quantity of $CaTiO_3$ (perovskite), all

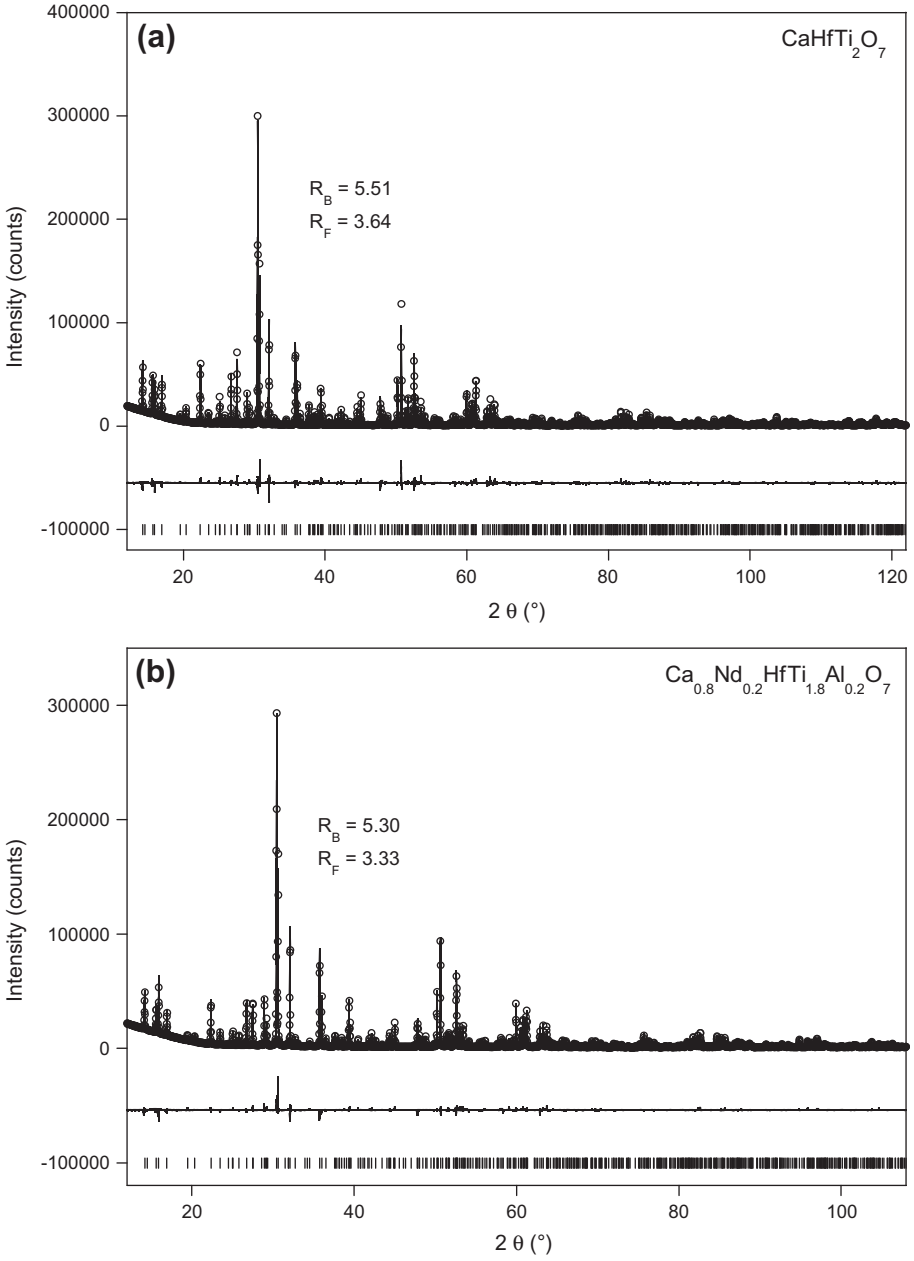

Fig. 2. XRD patterns ($\lambda K\alpha_1$(Cu) = 1.5406 Å) of the $Ca_{1-x}Nd_xHfTi_{2-x}Al_xO_7$, $x = 0$ (a) and 0.2 (b) ceramic samples. Experimental data (open circles) and Rietveld refinements (full line) are shown as well as their difference (shifted downwards) and the position of the lines (vertical bars). R_B and R_F are respectively the Bragg and the structure factors of Rietveld refinements.

Table 1
Lattice parameters (a, b, c, β) and cell volume obtained by XRD for Hf- and Zr-zirconolite ceramics. Numbers in parentheses are error standard deviations and apply to the last quoted place.

Ceramic samples	a (Å)	b (Å)	c (Å)	β (°)	Volume (Å^3)
$CaHfTi_2O_7$	12.42487(6)	7.27095(3)	11.36514(5)	100.5412(2)	1009.406(8)
$CaHfTi_2O_7$[a]	12.420	7.262	11.343	100.57	1005.71
$CaZrTi_2O_7$	12.4436(6)	7.2742(4)	11.3813(5)	100.554(4)	1012.8(9)
$Ca_{0.8}Nd_{0.2}HfTi_{1.8}Al_{0.2}O_7$	12.45438(6)	7.26699(3)	11.35141(5)	100.6546(1)	1009.657(8)
$Ca_{0.8}Nd_{0.2}ZrTi_{1.8}Al_{0.2}O_7$	12.4685(7)	7.2697(4)	11.3589(6)	100.654(5)	1011.9(11)

[a] Values reported by Vance et al. [47] for a $CaHfTi_2O_7$ prepared at 1450 °C using an alkoxide route.

the lines can be indexed in the monoclinic $C_{2/c}$ space group of the zirconolite-2M structure. The corresponding lattice parameters were determined by profile matching and are given in Table 1. In Table 1 are also reported the lattice parameters determined for the $CaZrTi_2O_7$ and $Ca_{0.8}Nd_{0.2}ZrTi_{1.8}Al_{0.2}O_7$ ceramics in previous works and prepared following the same method as the one used in the present paper [4,48,74]. It appears that the cell volume of the Hf-zirconolite ceramics ($x = 0$ and $x = 0.2$) is slightly lower than the one associated with the corresponding Zr-zirconolite ceramics. This result can be explained by the fact that Hf^{4+} cation radius is slightly smaller than Zr^{4+} one (respectively 0.78 Å and 0.76 Å in sevenfold coordination [46]). The incorporation of neodymium in both Hf- and Zr-zirconolite has no significant effect on cell volume. However, Nd induces an evolution of the a (increase) and c (decrease) parameters whereas b does not significantly change for Hf-zirconolite ceramics. These different results are in agreement with the ones we have already reported and discussed for Zr-zirconolite ceramics ($0 \leqslant x \leqslant 0.6$) [4,48,74]. Moreover, it can be noticed that our results concerning the lattice parameters of the $x = 0$ Hf-zirconolite ceramic are in agreement with the ones published in literature [47] (Table 1).

SEM shows that the three Hf-zirconolite samples are almost single-phase and confirms the occurrence of perovskite traces (Fig. 3) detected by XRD. Moreover, a (Hf, Ti)-rich minor phase heterogeneously distributed in the samples is also observed for the three samples (not shown in Fig. 3). The composition of the Hf-zirconolite phase was determined for $x = 0$ and $x = 0.2$ using EPMA (average of 9–10 measurements): $Ca_{0.99}Hf_{0.98}Ti_{2.00}O_7$ and $Ca_{0.797}Nd_{0.198}Hf_{0.998}Ti_{1.80}Al_{0.194}O_7$ respectively (the incorporation of both Nd and Al in the structure of the $x = 0.2$ sample is also shown on EDX spectra, Fig. 4a and b). It clearly appears that, despite the occurrence of minor phases in the samples, the composition of the Hf-zirconolite is very similar to the one expected. Because of the poor resolution of our EPMA apparatus, it was not possible to determine the composition of the minor phases by this technique. However, EDX spectra and analysis shows that:

- For the $x = 0$ ceramic (Fig. 4c), the composition of the perovskite phase $Ca_{0.97}Ti_{0.96}Hf_{0.02}O_3$ is close to the stoichiometric one.
- For the $x = 0.01$ ceramic, Nd is both incorporated in the zirconolite and perovskite phases.

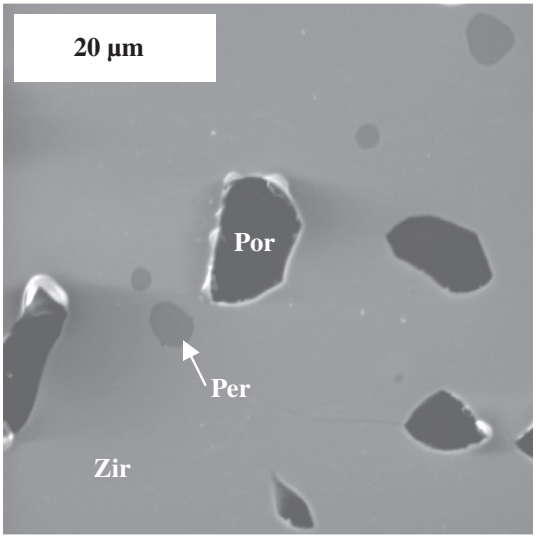

Fig. 3. Back-scattered electron image of the $Ca_{0.8}Nd_{0.2}HfTi_{1.8}Al_{0.2}O_7$ ceramic sample (Por: porosity, Per: perovkite, Zir: zirconolite).

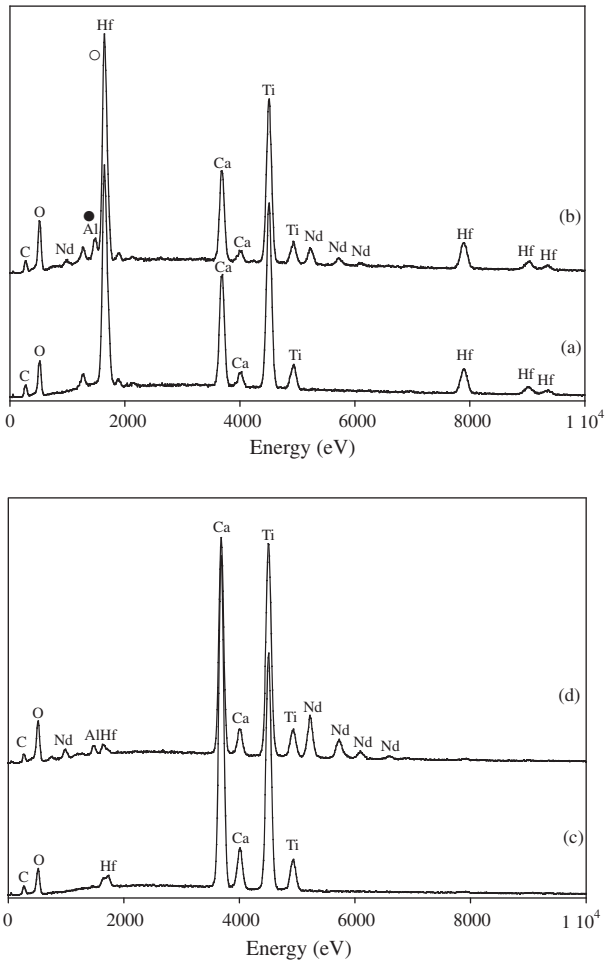

Fig. 4. EDX spectra of: (a) the Hf-zirconolite phase in the sample $x = 0$; (b) the Hf-zirconolite phase in the sample $x = 0.2$ showing the incorporation of both Nd and Al in the structure (due to the overlap between the strongest hafnium M lines (M_1(Hf) = 1645 eV, M_2(Hf) = 1698 eV) (○) and the aluminum Kα_1 line (Kα_1(Al) = 1487 eV) (●), it was not possible to determine correctly the composition of the Nd-doped ceramics by EDX); (c) the perovskite phase in the sample $x = 0$; (d) the perovskite phase in the sample $x = 0.2$.

– For the $x = 0.2$ ceramic, the perovskite phase incorporates both Nd, Al and Hf in its structure (Fig. 4d). But its composition was not determined due to the overlap between Al and Hf lines as indicated above.

In a previous work concerning Zr-zirconolite ceramics [48], the occurrence of the same kind of minor phases was also observed. In fact, the formation of perovskite as an intermediate phase during zirconolite synthesis seems to be difficult to avoid probably for kinetics reasons. This was demonstrated by Laverov et al. for Zr-zirconolite [78]. $CaTiO_3$ perovskite inclusions were also observed by Putnam et al. preparing Hf-zirconolite ceramics [64].

3.2. XRD Rietveld refinement

The structure of $Ca_{1-x}Nd_xHfTi_{2-x}Al_xO_7$ ($x = 0$ and $x = 0.2$) was refined by the Rietveld method using the Fullprof suite. The background was interpolated between a set of 93 points, a Thompson–Cox–Hastings peak shape was chosen, isotropic displacement factors were considered and the global composition was fixed at that corresponding to the nominal composition, which notably excluded the existence of vacancies. In the refinement procedure, the lattice parameters were first refined with the following parameters: cos(theta)-shift correction, background terms, peak shape parameters and low angle asymmetry correction. In the second step of the refinement, cell content was introduced (atomic positions, site occupancies) as well as isotropic displacement parameters and the scale factor. Due to the high number of intensity parameters (about 50), some constraints were introduced in order to reduce this number. Notably, the same isotropic displacement parameter was refined for all the oxygen sites; the same assumption was made for the two octahedral titanium sites (Ti(1) and Ti(3)).

The structural refinements were based on the $CaZr_{0.92}Ti_{2.08}O_7$ structure determination of Cheary [79]. Perovskite traces XRD lines (notably near 38.6° and 56°) were excluded from the XRD patterns for analysis. To determine site occupancies, coupled substitutions were considered between Ca site and Hf site on the one hand, and between Hf site and Ti(1), Ti(2) and Ti(3) sites on the other hand: such substitution are indeed known to occur in $CaZrTi_2O_7$ zirconolite-2M [38,67,79]. The results of the refinements are presented in Fig. 2, and in Tables 2–6. The satisfactory values of Bragg R factor ($R_B = 5.5$ for $CaHfTi_2O_7$ and $R_B = 5.3$ for $Ca_{0.8}Nd_{0.2}HfTi_{1.8}Al_{0.2}O_7$) confirms that the structure is of zirconolite-2M type.

3.3. ESR and optical studies

The ESR spectra of the $x = 0.01$ and $x = 0.2$ samples are shown in Fig. 5. For the lowly Nd-doped ceramic, the spectrum clearly indicates the existence of Fe^{3+} and V^{4+} paramagnetic impurities originating either from raw materials or from the pelletization process (Fig. 5a). These two impurities were already observed in the Zr-zirconolite ceramics [48]. Moreover, for the $x = 0.01$ sample, two other ESR signals are observed:

– A very wide one attributed to Nd^{3+} cations in the Hf-zirconolite structure. For this low neodymium concentration, this signal is relatively difficult to detect (Fig. 5a) due partly to the occurrence of the paramagnetic impurities but it dominates the spectrum for higher neodymium concentrations (Fig. 5b).
– A thinner one attributed to Nd^{3+} cations in an orthorhombic symmetry site in the perovskite minor phase (Fig. 5a). This signal is partly hidden by the one of vanadium impurities and is very similar to a signal already observed for lowly Nd-doped Zr-zirconolite ceramics [4]. This ESR signal can be attributed to Nd^{3+} cations in the calcium site of the perovskite minor phase by comparison with the one of a $Ca_{0.9}Nd_{0.1}Ti_{0.9}Al_{0.1}O_3$ perovskite ceramic sample (Fig. 6).

Consequently, for the $x = 0.01$ sample, Nd^{3+} cations are partitioned between the main crystalline phase (Hf-zirconolite) and the perovskite minor phase. These results are in accordance with

Table 2
Occupancies, atomic positions and isotropic displacement B factors determined from the Rietveld refinement of $CaHfTi_2O_7$ structure. Numbers in parentheses are error standard deviations and apply to the last quoted place.

Site	Site occupancy	Position	x	y	z	B (Å^2)
Ca	1 Ca	8f	0.3736(3)	0.1265(6)	0.4936(2)	0.33(5)
Hf	0.971(2)Hf + 0.029(2)Ti	8f	0.12295(6)	0.1225(1)	−0.02534(6)	0.19(1)
Ti(1)	0.971(2)Ti + 0.029(2)Hf	8f	0.2493(2)	0.1231(7)	0.7454(2)	0.23(5)
Ti(2)	0.5 Ti	8f	0.4711(4)	0.0480(6)	0.2506(7)	0.8(1)
Ti(3)	1 Ti	4e	0	0.1313(7)	0.25	0.23(5)
O(1)	1 O	8f	0.3096(6)	0.127(2)	0.2795(6)	0.16(7)
O(2)	1 O	8f	0.4756(7)	0.133(2)	0.1060(6)	0.16(7)
O(3)	1 O	8f	0.2082(7)	0.082(1)	0.5745(7)	0.16(7)
O(4)	1 O	8f	0.3991(7)	0.161(1)	0.7181(7)	0.16(7)
O(5)	1 O	8f	0.7032(7)	0.181(1)	0.5901(7)	0.16(7)
O(6)	1 O	8f	−0.0020(6)	0.130(1)	0.4148(6)	0.16(7)
O(7)	1 O	8f	0.1148(7)	0.046(1)	0.7992(7)	0.16(7)

Table 3
Bond distances Å determined from the Rietveld refinement of $CaHfTi_2O_7$ structure. The mean distance is indicated in the last line of the table. Numbers in parentheses are error standard deviations and apply to the last quoted place.

Ca		Hf		Ti(1)		Ti(2)		Ti(3)	
O(1)	2.418(7)	O(2)	2.26(1)	O(1)	1.96(1)	O(1)	2.17(1)	O(4)	1.954(9)
O(2)	2.360(9)	O(3)	2.049(8)	O(1)	1.98(1)	O(2)	1.76(1)	O(4)	1.954(9)
O(2)	2.49(1)	O(5)	2.070(8)	O(3)	1.938(8)	O(2)	1.77(1)	O(6)	1.877(7)
O(3)	2.410(9)	O(5)	2.443(9)	O(4)	1.961(9)	O(4)	1.768(9)	O(6)	1.877(7)
O(3)	2.42(1)	O(6)	2.130(8)	O(5)	1.902(8)	O(4)	2.197(9)	O(7)	1.926(9)
O(4)	2.525(8)	O(6)	2.421(9)	O(7)	1.964(9)			O(7)	1.926(9)
O(5)	2.544(9)	O(7)	2.056(8)						
O(6)	2.48(1)								
	2.456		2.204		1.951		1.929		1.919

Table 4
Occupancies, atomic positions and isotropic displacement B factors determined from the Rietveld refinement of $Ca_{0.8}Nd_{0.2}HfTi_{1.8}Al_{0.2}O_7$ structure. Numbers in parentheses are error standard deviations and apply to the last quoted place.

Site	Site occupancy	Position	x	y	z	B (Å^2)
Ca	0.8Ca + 0.2Nd	8f	0.3733(2)	0.1267(4)	0.4945(1)	0.29(3)
Hf	0.953(2)Hf + 0.047(2)Ti	8f	0.12176(6)	0.1248(1)	−0.02624(5)	0.24(1)
Ti(1)	0.953(2)Ti + 0.047(2)Hf	8f	0.2496(2)	0.1203(7)	0.7453(2)	0.76(5)
Ti(2)	0.368(5)Ti + 0.132(5)Al	8f	0.4684(5)	0.0515(6)	0.2505(6)	0.7(1)
Ti(3)	0.864(10)Ti + 0.136(10)Al	4e	0	0.1291(8)	0.25	0.76(5)
O(1)	1 O	8f	0.3006(5)	0.123(2)	0.2824(6)	0.17(6)
O(2)	1 O	8f	0.4674(6)	0.125(2)	0.1053(6)	0.17(6)
O(3)	1 O	8f	0.2048(6)	0.089(1)	0.5730(6)	0.17(6)
O(4)	1 O	8f	0.4006(7)	0.170(1)	0.7142(6)	0.17(6)
O(5)	1 O	8f	0.7016(7)	0.179(1)	0.5902(6)	0.17(6)
O(6)	1 O	8f	−0.0043(6)	0.116(1)	0.4127(6)	0.17(6)
O(7)	1 O	8f	0.1148(7)	0.058(1)	0.7967(6)	0.17(6)

Table 5
Bond distances Å determined from the Rietveld refinement of $Ca_{0.8}Nd_{0.2}HfTi_{1.8}Al_{0.2}O_7$ structure. The mean distance is indicated in the last line of the table. Numbers in parentheses are error standard deviations and apply to the last quoted place.

Ca		Hf		Ti(1)		Ti(2)		Ti(3)	
O(1)	2.410(7)	O(2)	2.23(1)	O(1)	1.93(1)	O(1)	2.258(9)	O(4)	1.906(9)
O(2)	2.34(1)	O(3)	2.081(8)	O(1)	1.94(1)	O(2)	1.73(1)	O(4)	1.906(9)
O(2)	2.459(8)	O(5)	2.072(7)	O(3)	1.945(7)	O(2)	1.765(9)	O(6)	1.860(7)
O(3)	2.348(9)	O(5)	2.472(9)	O(4)	2.010(9)	O(4)	1.832(9)	O(6)	1.860(7)
O(3)	2.442(8)	O(6)	2.122(8)	O(5)	1.902(7)	O(4)	2.276(9)	O(7)	1.974(9)
O(4)	2.475(7)	O(6)	2.365(9)	O(7)	1.930(9)			O(7)	1.974(9)
O(5)	2.527(8)	O(7)	2.053(7)						
O(6)	2.577(9)								
	2.454		2.200		1.943		1.972		1.913

Table 6
Ca–Ti bond distances determined from the Rietveld refinement of $CaHfTi_2O_7$ and $Ca_{0.8}Nd_{0.2}HfTi_{1.8}Al_{0.2}O_7$ structure.

$CaHfTi_2O_7$		$Ca_{0.8}Nd_{0.2}HfTi_{1.8}Al_{0.2}O_7$	
Ca–Ti(1)	3.39 Å	Ca–Ti(1)	3.40 Å
	3.47 Å		3.46 Å
	3.49 Å		3.48 Å
Ca–Ti(2)	3.21 Å	Ca–Ti(2)	3.20 Å
	3.26 Å		3.25 Å
	3.43 Å		3.44 Å
	3.70 Å		3.73 Å
Ca–Ti(3)	3.52 Å	Ca–Ti(3)	3.52 Å

EDX ones. Thus, both for Hf- and Zr-zirconolite, neodymium cations have a strong tendency to be incorporated in the perovskite traces which is in accordance with the results reported by Lumpkin et al. [80] on rare earth cations distribution between Zr-zirconolite and perovskite phases in multiphase Synroc samples which showed that the big trivalent rare earth cations such as cerium and neodymium preferentially enter the big calcium site in perovskite structure (eightfold coordinated site with an average Ca–O distance of 2.64 Å) than the small calcium site in Zr-zirconolite structure (eightfold coordinated site with an average Ca–O distance of 2.45 Å). For the $x = 0.2$ sample, the ESR spectrum (Fig. 5b) is associated with Nd^{3+} cations located in the calcium site of the Hf-zirconolite structure and is very similar to the one observed for the Zr-zirconolite $Ca_{0.8}Nd_{0.2}ZrTi_{1.8}Al_{0.2}O_7$ ceramic [48,74]. At least two components S_1 (the strongest one) and S_2 (the smallest one) are needed to simulate the spectrum and correspond to Nd^{3+} cations located in two slightly different calcium sites probably due to differences concerning the location and the nature of second neighbors (see Section 4). Their simulation parameters (g_1, g_2, g_3) and the corresponding half-width at half-maximum ($\Delta_1, \Delta_2, \Delta_3$), using orthorhombic g tensors (which can be justified because of the low symmetry of the calcium site in the zirconolite structure) are given in Table 7. Nevertheless, the determination of the ESR parameters associated with the low intensity S_2 signal are not as accurate as the one determined for the S_1 signal. The relative proportions of sites S1 and S2 have been determined by double integration of the corresponding simulated spectra: S1 (86%) and S2 (14%). These values show that Nd^{3+} cations are majoritarily located in S1 sites. The comparison of Nd-doped Hf- and Zr-zirconolite ESR parameters (Table 7) shows that the environments of Nd^{3+} cations in these two ceramics are very similar which is in accordance with the XRD results. Moreover, the relative proportions of sites S1 and S2 in the $Ca_{0.8}Nd_{0.2}ZrTi_{1.8}Al_{0.2}O_7$ Zr-zirconolite ceramic (S1 (87%) and S2 (13%)) [74] are also very close to that determined for the $Ca_{0.8}Nd_{0.2}HfTi_{1.8}Al_{0.2}O_7$ ceramic. All these ESR results show that the substitution of Zr by Hf in zirconolite composition only slightly affect the environment and the distribution of Nd^{3+} cations in the structure.

The optical absorption spectra ($^4I_{9/2} \rightarrow {}^2P_{1/2}$ transition) of the Hf-zirconolite $Ca_{0.8}Nd_{0.2}HfTi_{1.8}Al_{0.2}O_7$ ceramic recorded at low temperature ($T \approx 10$ K) is shown in Fig. 7a. Three relatively wide width (half-width at half-maximum $\Delta \approx 25$–30 cm^{-1}) Gaussian shape components (G_1, G_2, and G_3) occurring respectively at 23,091, 23,120 and 23,141 cm^{-1} are needed to simulate this spectrum. The comparison of optical absorption spectra recorded at 10 and 300 K (Fig. 8) shows that the component G_1 occurring at the lowest energy (23,091 cm^{-1}) is not due to a $^4I_{9/2} \rightarrow {}^2P_{1/2}$ transition from a thermally populated Stark level (Fig. 7b). Moreover, the fact that the same three components are observed on the spectrum of a Zr-zirconolite $Ca_{0.93}Nd_{0.07}ZrTi_{1.93}Al_{0.07}O_7$ single crystal (Table 8) clearly demonstrates that the components G_1, G_2 and G_3 observed for the $Ca_{0.8}Nd_{0.2}HfTi_{1.8}Al_{0.2}O_7$ ceramic are all due to Nd^{3+} cations located in Hf-zirconolite crystals and not in the perovskite minor phase. In addition, in other works [74] performed on a Nd-doped Zr-zirconolite $Ca_{0.95}Nd_{0.1}Zr_{0.95}Ti_2O_7$ ceramic it was shown that

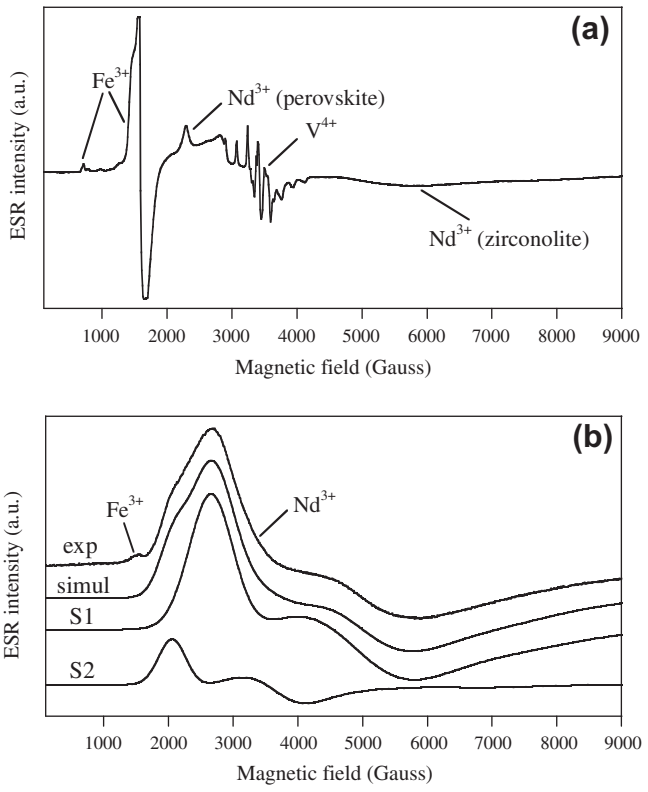

Fig. 5. ESR spectra of the $Ca_{1.99}Nd_{0.01}HfTi_{1.99}Al_{0.01}O_7$ (a) and $Ca_{0.8}Nd_{0.2}HfTi_{1.8}Al_{0.2}O_7$ (b) ceramics recorded at 12 K (X-band, microwave frequency $\nu = 9.49$ GHz). For the $Ca_{1.99}Nd_{0.01}HfTi_{1.99}Al_{0.01}O_7$ ceramic sample, Nd^{3+} cations are detected both in perovskite (minor phase) and in zirconolite (very wide signal of low intensity). The presence of paramagnetic impurities (Fe^{3+} and V^{4+} cations) is also easily detected for this sample due to the low concentration of Nd^{3+} cations. For the $Ca_{0.8}Nd_{0.2}HfTi_{1.8}Al_{0.2}O_7$ ceramic, Nd^{3+} cations spectrum was simulated using two types of sites S1 and S2 to account for the shoulder at approximately 2100 G observed on the experimental spectrum (the corresponding g values are reported in Table 7). The relative proportions of sites S1 and S2 have been determined by double integration of the corresponding simulated spectra: S1 (86%) and S2 (14%). The global simulated spectrum (simul) corresponding to S1 + S2 ESR signals is also shown for comparison with the experimental spectrum (exp).

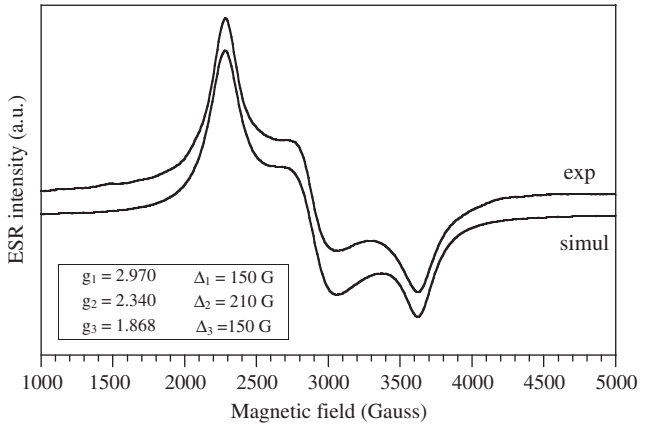

Fig. 6. ESR spectrum of neodymium in a $Ca_{0.9}Nd_{0.1}Ti_{0.9}Al_{0.1}O_3$ perovskite ceramic sample recorded at 12 K (X-band, microwave frequency $\nu = 9.49$ GHz). The spectrum was simulated using an orthorhombic g-tensor. The simulation parameters (g_1, g_2, g_3) and the corresponding half-width at half-maximum ($\Delta_1, \Delta_2, \Delta_3$) are given in the figure. Simul: simulated spectrum; Exp: experimental spectrum.

the $^4I_{9/2} \rightarrow {}^2P_{1/2}$ transition ($T \approx 10$ K) of Nd^{3+} cations located in the zirconium site occurred around 22,950 cm^{-1} which confirms that

Table 7
Main components (g_1, g_2, g_3) of the g-tensor and corresponding half-width at half-maximum ($\Delta_1, \Delta_2, \Delta_3$) determined after simulation of the ESR spectrum of the Hf-zirconolite $Ca_{0.8}Nd_{0.2}HfTi_{1.8}Al_{0.2}O_7$ ceramic using the contribution of two signals S_1(Hf) and S_2 (Hf) (Fig. 5). The values obtained for the Zr-zirconolite $Ca_{0.8}Nd_{0.2}ZrTi_{1.8}Al_{0.2}O_7$ ceramic (simulation of the ESR spectrum using the contribution of two signals S_1(Zr) and S_2(Zr)) are given for comparison [74]. All simulations were performed using Gaussian shape curves.

	g_1	Δ_1 (Gauss)	g_2	Δ_2 (Gauss)	g_3	Δ_3 (Gauss)
S_1(Hf)	0.90	2200	1.35	1500	2.48	665
S_2(Hf)	0.95	1300	1.83	800	3.25	420
S_1(Zr)	0.84	2400	1.30	1800	2.46	660
S_2(Zr)	0.80	1800	1.73	1100	3.21	400

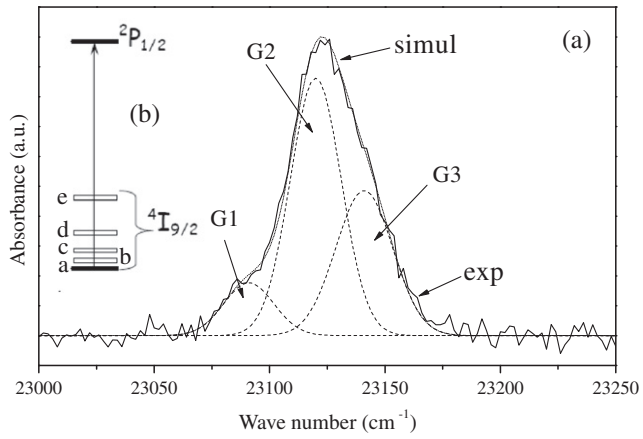

Fig. 7. (a) Optical absorption spectrum (exp) of neodymium in the $Ca_{0.8}Nd_{0.2}HfTi_{1.8}Al_{0.2}O_7$ ceramic recorded at $T \approx 10$ K ($^4I_{9/2} \rightarrow {}^2P_{1/2}$ transition). The simulated spectrum (simul) was obtained using three Gaussian shape components G_1, G_2 and G_3 (see Table 8). (b) Scheme showing the transition from the lowest Stark level of the $^4I_{9/2}$ state to the non-degenerated $^2P_{1/2}$ excited state. The $^4I_{9/2}$ ground state of neodymium cation is splitted into five Stark (or Kramers) a, b, c, d and e doublets under the action of a low symmetry crystal field (this is the case for Nd^{3+} cations in the calcium site of C_1 symmetry in Hf- and Zr-zirconolite). At $T \approx 10$ K only the lowest Stark doublet a of the $^4I_{9/2}$ state is populated. As the degeneracy of the $^2P_{1/2}$ state is not removed by the crystal field occurring around Nd^{3+} cations, each kind of neodymium environment is characterized by only one absorption band $^4I_{9/2} \rightarrow {}^2P_{1/2}$ at low temperature.

none of the three components observed in Fig. 7a is due to a fraction of neodymium cations located in the hafnium site. The same line position is indeed expected for Nd-doped Hf-zirconolite as the mean Hf–O (2.22 Å) and Zr–O (2.20 Å) distances are very similar. All these considerations show that three different neodymium environments in the calcium site of the Hf-zirconolite structure are detected using optical absorption spectroscopy. The same number of components with very similar parameters was obtained by simulation of the $^4I_{9/2} \rightarrow {}^2P_{1/2}$ absorption band for a $Ca_{0.9}Nd_{0.1}ZrTi_{1.9}Al_{0.1}O_7$ ceramic sample (Table 8) [74] This indicates that the environment of Nd^{3+} cations is very similar in Hf- and Zr-zirconolite which is in agreement with our ESR results (Table 7). However, by optical absorption spectroscopy, an additional site is detected for neodymium both in Hf- and Zr-zirconolite. This difference between the results obtained using these two techniques can be explained by the fact that the ESR spectrum of Nd^{3+} cations in zirconolite (Fig. 5b) is very anisotropic (indeed, the main components of the g tensors range from 0.84 to 3.25, Table 7) and the Δ_1, Δ_2 and Δ_3 values are very large (Table 7) in comparison with the optical absorption spectrum (Fig. 7a). If it is assumed that the oscillator strength (linked to the transition probability) of the individual $^4I_{9/2} \rightarrow {}^2P_{1/2}$ transitions does not significantly vary from one Nd environment to another (due to the occupancy of the same

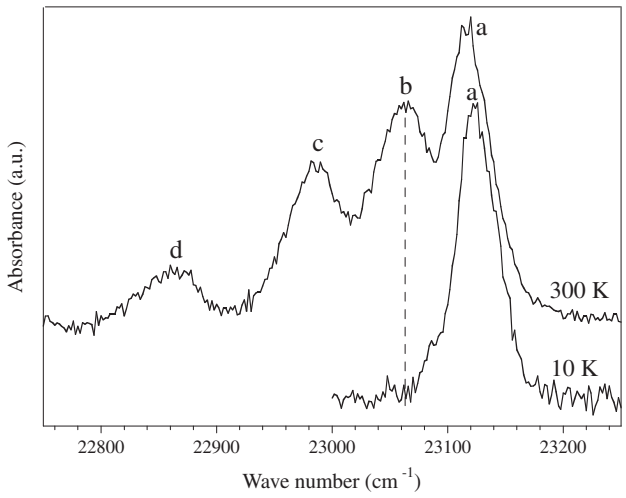

Fig. 8. Comparison of the optical absorption spectrum ($^4I_{9/2} \rightarrow {}^2P_{1/2}$ transition) of neodymium in the $Ca_{0.8}Nd_{0.2}HfTi_{1.8}Al_{0.2}O_7$ ceramic recorded at 10 and 300 K. The four bands referred to as a, b, c and d on the spectrum recorded at 300 K correspond respectively to transitions from the a, b, c and d Stark levels (see Fig. 7b) to the $^2P_{1/2}$ excited state. At 10 K only the transition from the lowest Stark level of the $^4I_{9/2}$ state to the $^2P_{1/2}$ state is observed and no contribution of the second Stark level (level b in Fig. 7b) is detected. A slight shift of the position of band a towards higher energy is observed when the temperature decreases and can probably be explained by contraction of the zirconolite structure (decrease of the average Nd–O distance leading to an increase of the average crystal field around Nd^{3+} cations).

basic calcium site in all cases), the area ratio of the absorption bands G_1, G_2 and G_3 can be used to estimate the relative amounts of Nd^{3+} cations located in the three different environments. Table 8 shows that the distribution of neodymium in the different environments is very similar for Hf- and Zr-zirconolite. The components G_2 and G_3 observed optically and that exhibit the closest parameters (Table 8) are probably unresolved by ESR and may correspond to the strong component S_1 (Fig. 5b). The comparison of the relative surface area of the S_1 component on one hand (86% for Hf-zirconolite and 87% for Zr-zirconolite) with the relative surface area of the $G_2 + G_3$ components on the other hand (89% for Hf-zirconolite and 82.8% for Zr-zirconolite) seems to confirm this hypothesis. Moreover, it must be underlined that the Nd^{3+} cations optical absorption line width in zirconolite ($\Delta \approx 25$–$30\ cm^{-1}$) is relatively large in comparison with other crystalline materials such as Nd-doped $Y_3Al_5O_{12}$ (YAG) for which Δ does not exceed several cm^{-1} at low temperature [81]. This indicates that in zirconolite the neodymium absorption line width is strongly inhomogeneously broadened which can be explained by a disorder in the Nd^{3+} cations environment (see Section 4 in the next part).

In Fig. 9b is reported the evolution of the fluorescence spectra ($T < 20$ K) from the lowest Stark level of the $^4F_{3/2}$ state to the highest Stark level of the $^4I_{9/2}$ state (see arrow (2) in Fig. 9a) of Nd^{3+} cations in the $Ca_{0.99}Nd_{0.01}HfTi_{1.99}Al_{0.01}O_7$ ceramic after selective excitation at the exciting wavelength λ_{ex} in the $^4I_{9/2} \rightarrow {}^4F_{3/2}$ low energy absorption band (Fig. 10). This fluorescence transition was chosen because it is clearly separated from the other transitions to the four lowest Stark levels of the $^4I_{9/2}$ state (Fig. 11). In these conditions, only one $^4F_{3/2} \rightarrow {}^4I_{9/2}$ fluorescence band is expected for each kind of neodymium environment. However, Fig. 9b clearly shows that the value of the exciting wavelength λ_{ex} has a strong effect on the fluorescence spectra and more particularly on the number of components observed. For instance, for $\lambda_{ex} = 878.92$ nm, at least five individual components are needed to simulate the fluorescence spectra. This confirms once again that there is a distribution of neodymium environments in Hf-zirconolite. The estimation of the mean splitting energy values between the five Stark levels of the $^4I_{9/2}$ ground state of Nd^{3+} cations in the $Ca_{0.99}Nd_{0.01}HfTi_{1.99}Al_{0.01}O_7$ ceramic was performed using the fluorescence spectrum recorded at $T < 20$ K under an argon laser excitation ($\lambda_{ex} = 514.53$ nm). Fig. 11a shows the five bands corresponding to the fluorescence from the $^4F_{3/2}$ state and the energy splitting values are given in Fig. 11b. In this figure, the values obtained for Zr-zirconolite are also reported [74]. The comparison of the values obtained for the Hf- and Zr-ceramics clearly indicates that the effect of the crystal field on the splitting of the neodymium $^4I_{9/2}$ state is very similar in the two matrices which confirms the absence of significant effect of the replacement of Zr by Hf in the zirconolite structure and more particularly on Nd^{3+} cations environment. Fig. 11 also indicates that the separation between the two lowest Stark levels at $T < 20$ K is about $45\ cm^{-1}$ in Hf-zirconolite. In this temperature range, the thermal energy available is lower than $15\ cm^{-1}$ which is too low to populate the second Stark level (Fig. 11b). Consequently, this result confirms our assumption that the absorption spectra recorded at low temperature (Fig. 7) only correspond to transitions from the lowest Stark level of the $^4I_{9/2}$ state.

4. Discussion

4.1. Structure of Hf-zirconolite

The structure of $Ca_{1-x}Nd_xHfTi_{2-x}Al_xO_7$ ($x = 0$ and $x = 0.2$), which was determined by the Rietveld method, is similar to the one of $CaZrTi_2O_7$ zirconolite-2M (Tables 2–6). Nevertheless, the results show some subtle modifications of the structure between the two $Ca_{1-x}Nd_xHfTi_{2-x}Al_xO_7$ ($x = 0$ and $x = 0.2$) samples.

From site occupancy refinements, it appeared that (Tables 2 and 4):

- In $CaHfTi_2O_7$, no substitution between Ca and Hf occurs but some Hf^{4+} ions enter preferentially the biggest Ti(1) site. The refinement would allow some Hf^{4+} ions in split Ti(2) site, but it comes to a sharp increase of displacement Ti(2) factor over $2\ Å^2$ without any significant improvement about the goodness of the fit: as a consequence this substitution mechanism was not further considered.
- In $Ca_{0.8}Nd_{0.2}HfTi_{1.8}Al_{0.2}O_7$, Nd^{3+} ions only enter into the eightfold coordinated Ca site and not into Hf site, in accordance with the comparison of the ionic radii: Ca^{2+} and Nd^{3+} have very similar ionic radii whereas Hf^{4+} ions are significantly smaller ($r(Nd^{3+}) = 1.109$ Å, $r(Ca^{2+}) = 1.12$ Å and $r(Hf^{4+}) = 0.83$ Å in eight-

Table 8
Parameters used for the simulation of the optical absorption spectrum ($^4I_{9/2} \rightarrow {}^2P_{1/2}$ transition, $T \approx 10$ K) of the Hf-zirconolite $Ca_{0.8}Nd_{0.2}HfTi_{1.8}Al_{0.2}O_7$ ceramic with three Gaussian shape components G_1(Hf), G_2(Hf) and G_3(Hf) (see Fig. 7): E (position of the maximum), Δ (half-width at half-maximum), Area% (contribution of the component to the total surface area of the simulated spectrum). The corresponding values obtained after simulation with three Gaussian shape components of neodymium optical absorption spectra of a Zr-zirconolite $Ca_{0.9}Nd_{0.1}ZrTi_{1.9}Al_{0.1}O_7$ ceramic (G_1(Zr), G_2(Zr), G_3(Zr)) and of a Zr-zirconolite $Ca_{0.93}Nd_{0.07}ZrTi_{1.93}Al_{0.07}O_7$ single crystal (G'_1(Zr), G'_2(Zr), G'_3(Zr)) are given for comparison [74]. The Nd-doped Zr-zirconolite single crystal was prepared by slow cooling of a $CaO–ZrO_2–TiO_2–Al_2O_3–Nd_2O_3$ melt from 1600 °C to 1350 °C at 0.04 °C/min and from 1350 °C to room temperature at 4 °C/min [74].

	G_1(Hf)	G_2(Hf)	G_3(Hf)	G_1(Zr)	G_2(Zr)	G_3(Zr)	G'_1(Zr)	G'_2(Zr)	G'_3(Zr)
E (cm^{-1})	23,091	23,120	23,141	23,085	23,118	23,138	23,091	23,117	23,137
Δ (cm^{-1})	25.5	26	29	41	24	29	25	19	25
Area (%)	11	54.7	34.3	17.2	48	34.8	13.3	50.9	35.8

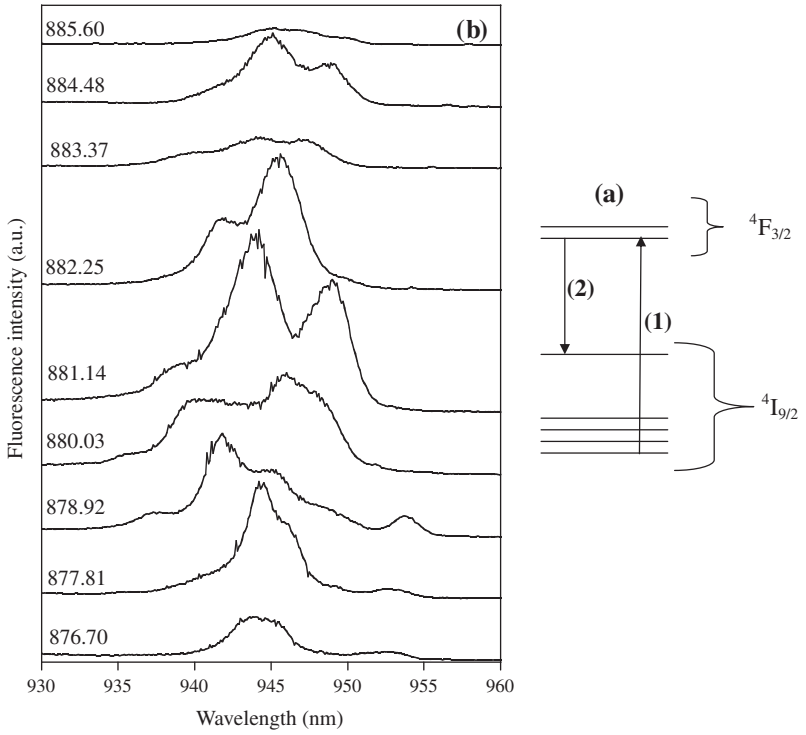

Fig. 9. (a) Scheme showing the excitation from the lowest Stark level of the $^4I_{9/2}$ ground state to the lowest Stark level of the doubly degenerated $^4F_{3/2}$ excited state (arrow (1)) and the fluorescence from the lowest Stark level of the $^4F_{3/2}$ state to the highest Stark level of the $^4I_{9/2}$ state (arrow (2)). (b) Line-narrowed fluorescence spectra ($T < 20$ K) of Nd^{3+} cations in $Ca_{0.99}Nd_{0.01}HfTi_{1.99}Al_{0.01}O_7$ ceramic. Transition from the lowest Stark level of the $^4F_{3/2}$ state (the only emitting level at low temperature) to the highest Stark level of the $^4I_{9/2}$ state (arrow (2) in (a)). The selective excitation was performed in the $^4I_{9/2} \rightarrow {}^4F_{3/2}$ absorption band (876–885 nm, arrow (1) in (a) and Fig. 10) and the corresponding excitation wavelengths are indicated in nm in the figure.

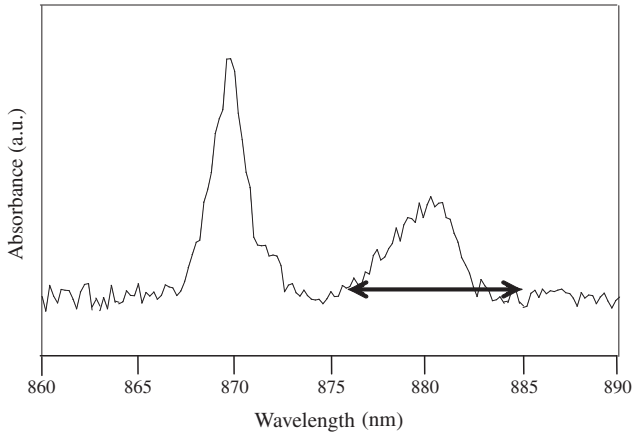

Fig. 10. Optical absorption spectrum ($^4I_{9/2} \rightarrow {}^4F_{3/2}$ transition) of neodymium in $Ca_{0.99}Nd_{0.01}HfTi_{1.99}Al_{0.01}O_7$ ceramic recorded at $T = 10$ K. The arrow indicated in the figure corresponds to the wavelength range used for the selective excitation in the lowest Stark level of the $^4F_{3/2}$ state (Fig. 9).

fold coordination [46]). Al^{3+} ions mainly occupy the split five-fold coordinated Ti(2) site, but almost one third of them also lie in the smallest Ti(3) titanium site.

As compared to the structural results of $CaHfTi_2O_7$ ($x = 0$), it seems that the coupled (Nd^{3+}, Al^{3+}) substitution introduces several structural changes (Tables 3 and 5):

- All the polyhedrons are slightly more distorted in $Ca_{0.8}Nd_{0.2}HfTi_{1.8}Al_{0.2}O_7$ than in $CaZrTi_2O_7$ (larger range of distances), although average cation – oxygen distances are not significantly modified. This latter fact probably explains why cell volume remains almost the same between $x = 0$ and $x = 0.2$ (Table 1).
- Ti(2) site seems to be the most sensitive to the coupled (Nd^{3+}, Al^{3+}) substitution. This could be a consequence of its preferential occupancy by Al^{3+} ions, which have a smaller ionic radius than Ti^{4+} ions ($r(Al^{3+}) = 0.48$ Å and $r(Ti^{4+}) = 0.51$ Å in five-fold coordination [46]). The split character of Ti(2) site is likely to give it a good ability to accommodate easily ionic radius variations. Moreover, as a result of its occupancy by Al^{3+} ions, an increase of the distance between the two split closest Ti(2)–Ti(2) sites, symmetrical by the twofold axis (located in $x = 0.5$ and $z = 0.25$), is observed: this distance is 0.72 Å for $x = 0$ and 0.79 Å for $x = 0.2$. Finally, it is noticeable that the preferential occupancy of Ti(2) site by Al^{3+} ions is in agreement with the fact that this site is the one which experiences the nearest distances to the Ca site where Nd^{3+} ions lie (Table 6): this could help to stabilize the structure by facilitating the local electroneutrality of the structure.
- When considering atomic displacement factors, the value for Ti(2) site is quite large even in $CaHfTi_2O_7$. It is likely that this value reflects the disorder due to the split character of this site as well as a broader distribution around its mean location. In $Ca_{0.8}Nd_{0.2}HfTi_{1.8}Al_{0.2}O_7$, atomic displacement factors related to Ti(1) and Ti(3) sites slightly increase, probably as a result of their partial occupation by Hf^{4+} and Al^{3+} ions.

4.2. Distribution of neodymium cations environment in Hf-zirconolite

Using ESR, optical absorption and luminescence spectroscopies sensitive to neodymium environment we showed above that in spite of the existence of only one crystallographic site for calcium (Fig. 1b) – and thus also for neodymium – in Hf-zirconolite $Ca_{1-x}Nd_xHfTi_{2-x}Al_xO_7$ ($x = 0.2$), between two and five different Nd environments were needed to simulate the spectra. It is important to underline that for the $x = 0.2$ sample, none of the optical absorp-

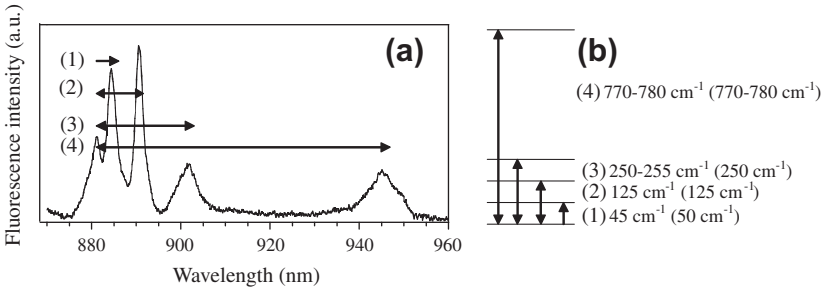

Fig. 11. (a) Fluorescence spectra ($T < 20$ K) of Nd^{3+} cations in $Ca_{0.99}Nd_{0.01}HfTi_{1.99}Al_{0.01}O_7$ ceramic from the lowest Stark level of the $^4F_{3/2}$ state to the five Stark levels of the $^4I_{9/2}$ ground state (see Fig. 9a) after excitation in the $^4I_{9/2} \rightarrow {}^4G_{92}$, $^2K_{13/2}$ region of the absorption spectrum with an argon laser (514.53 nm). (b) Estimation of the mean splitting energy values between the $^4I_{9/2}$ state Stark levels of neodymium in $Ca_{0.99}Nd_{0.01}HfTi_{1.99}Al_{0.01}O_7$ ceramic. The values given in parenthesis correspond to the ones determined for Nd in Zr-zirconolite [74].

tion bands and ESR signals observed can be attributed neither to Nd^{3+} cations located in the Hf site of the Hf-zirconolite structure nor to Nd^{3+} cations located in perovskite traces. A probable origin of this disorder around neodymium cations which would explain the occurrence of more than one environment for neodymium in the calcium site of Hf-zirconolite can be proposed as follows. The structural data obtained by XRD patterns Rietveld refinement of Nd-doped Hf-zirconolite in this paper and of Nd-doped Zr-zirconolite in previous works [4,48] clearly show that the Nd^{3+} cations located in the Ca site have two Ti(2) split sites in their next nearest neighborhood (Figs. 1 and 12). These four Ti(2) positions are located at different distances from the Nd^{3+} cations (Table 6, Fig. 12) and are statistically occupied by (Ti^{4+}/Al^{3+}) cations (50%) and vacancies (50%). Consequently, it appears that the environment of neodymium cations (and thus the crystal field around them) in the calcium site can vary from one site to another. About the localization of the second neighbors around Nd^{3+} ions, four environments must be considered due to the Ti(2) split character. For each of these localizations, the potential occupancy of Ti(2) and Ti(3) sites by Al^{3+} ions, as shown by Rietveld refinement, is then to be considered. From a pure statistical point of view, 0 to 3 Al^{3+} ions can surround each Nd^{3+} ions. With a statistical distribution of Al^{3+} ions among Ti(2) and Ti(3) sites for the $x = 0.2$ composition ($Ca_{0.8}Nd_{0.2}HfTi_{1.8}Al_{0.2}O_7$), about 51% of Nd^{3+} ions should experience 0 Al^{3+} ion in their second neighborhood, 38% 1 Al^{3+} ion, 10% 2 Al^{3+} ions, and 1% 3 Al^{3+} ions. Both the localization and the nature of the second neighbors influence the crystal field experienced by Nd^{3+} ions. Then a multisite and an inhomogeneous broadening of Nd^{3+} spectroscopic lines is expected, but it is difficult to determine which parameter (localization or/and occupancy) is the most important to explain the number of broad lines which is observed in ESR or optical spectroscopies. This will require comparing at least several samples with different Nd^{3+} substitution levels.

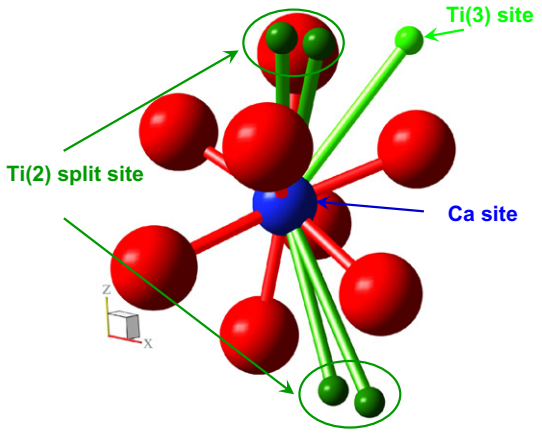

Fig. 12. Local Hf-zirconolite $Ca_{0.8}Nd_{0.2}HfTi_{1.8}Al_{0.2}O_7$ structure showing the positions of the nearest Ti sites from the (Ca, Nd) site (eightfold coordinated by oxygen atoms) likely to be occupied by Al^{3+} ions. Each pair of close Ti(2) positions are statistically occupied (50–50%) either by Ti^{4+} and Al^{3+} cations, or by vacancies.

5. Conclusion

In this work we prepared and studied the structure of Nd-doped Hf-zirconolite ($Ca_{1-x}Nd_xHfTi_{2-x}Al_xO_7$, $x = 0$; 0.01 and 0.2) ceramics. XRD and SEM showed that almost single-phase samples were obtained by the solid state reaction method used in this study (only small amounts of perovskite ($CaTiO_3$) and of a (Hf, Ti)-rich minor phase have been detected). The lattice parameters and the cell volume of Hf-zirconolite ceramics were only slightly smaller than those of Zr-zirconolite because Hf^{4+} cation is slightly smaller than Zr^{4+} cation. Nevertheless, no significant effect of replacement of Zr by Hf was observed on the zirconolite-2M structure: Rietveld refinements revealed that Nd^{3+} ions only enter the Ca site of the structure, whereas part of Hf^{4+} ions substitute titanium into Ti(1) sites and Al^{3+} ions mainly occupy the Ti(2) split sites and Ti(3) sites. Using spectroscopic techniques (ESR, optical absorption and fluorescence spectroscopies), it was shown that between two and five local environments of neodymium cations and large optical and ESR bandwidths were detected in Hf-zirconolite ceramics, which can be attributed to the existence of an important disorder in the neighborhood of the Ca site containing Nd. The existence of this disorder around Nd^{3+} cations is probably due to the statistical occupancy of the split Ti(2) site (which is the next nearest cationic site of neodymium) both by Ti^{4+} and Al^{3+} cations and by vacancies. Moreover, 0–3 Al^{3+} ions can potentially surround each Nd^{3+} ion. In accordance with XRD results, no significant differences were observed concerning the neodymium cations environment and distribution between Hf- and Zr-zirconolite ceramics. For instance, the effect of crystal field on the splitting of the neodymium $^4I_{9/2}$ ground state was very similar for the two matrices. The replacement of Zr by Hf in ceramic composition has thus no significant effect on zirconolite structure and on Nd^{3+} cations environment.

Acknowledgment

The Commissariat à l'Energie Atomique (CEA, France) is gratefully acknowledged for its financial support.

References

[1] C. Madic, M. Lecomte, P. Baron, B. Boullis, C. R. Phys. 3 (2002) 797–811.
[2] D. Warin, Mater. Res. Symp. Proc. 985 (2007) 613–620.
[3] A.V. Ochkin, S.V. Stefanosky, S.I. Rovny, Mater. Res. Soc. Symp. Proc. 757 (2003) 315–319.

[4] D. Caurant, P. Loiseau, O. Majérus, V. Aubin-Chevaldonnet, I. Bardez, A. Quintas, Glasses, Glass–Ceramics and Ceramics for Immobilization of Highly Radioactive Nuclear Wastes, Nova Science Publishers (Ed.), New York, 2009.
[5] W.E. Lee, M.I. Ojovan, M.C. Stennett, N.C. Hyatt, Adv. Appl. Ceram. 105 (2006) 3–12.
[6] I.W. Donald, B.L. Metcalfe, R.N.J. Taylor, J. Mater. Sci. 32 (1997) 5851–5887.
[7] C. Guy, F. Audubert, J-E. Lartigue, C. Latrille, T. Advocat, C. Fillet, C. R. Phys. 3 (2002) 827–837.
[8] C. Fillet, T. Advocat, F. Bart, G. Leturcq, H. Rabiller, C. R. Chim. 7 (2004) 1165–1172.
[9] 9] P. Loiseau, D. Caurant, N. Baffier, L. Mazerolles, C. Fillet, J. Nucl. Mater. 335 (2004) 14–32.
[10] D. Caurant, O. Majérus, P. Loiseau, I. Bardez, N. Baffier, J.L. Dussossoy, J. Nucl. Mater. 354 (2006) 143–162.
[11] M.I. Ojovan, W.E. Lee, An Introduction to Nuclear Waste Immobilisation, Elsevier (Ed.), Oxford, 2005. pp. 213–267.
[12] E. Vance, Mater. Res. Soc. Symp. Proc. 985 (2007) 137–144.
[13] M.I. Ojovan, W.E. Lee, New Developments in Glassy Nuclear Wasteforms, Nova Science Publishers (Ed.), New York, 2007.
[14] I.W. Donald, Waste Immobilization in Glass and Ceramic based Hosts. Radioactive, Toxic and Hazardous Wastes, Wiley (Ed.), Chichester, United Kingdom, 2010.
[15] S.V. Stefanovsky, S.V. Yudintsev, R. Giéré, G.R. Lumpkin, Nuclear waste forms, in: R. Giéré, P. Stille (Eds.), Energy, Waste and the Environment: A Geochemical Perspective, vol. 236, Geochemical Society, London, 2004, pp. 37–63 (Special publications).
[16] D.M. Strachan, R.D. Scheele, E.C. Buck, J.P. Icenhower, A.E. Kozelisky, R.L. Sell, R.J. Elovich, W.C. Buchmiller, J. Nucl. Mater. 345 (2005) 109–135.
[17] M.C. Stennett, E.R. Maddrell, C.R. Scales, F.R. Livens, M. Gilbert, N.C. Hyatt, Mater. Res. Soc. Symp. Proc. 985 (2007) 145–150.
[18] M.C. Stennett, N.C. Hyatt, M. Gilbert, F.R. Livens, E.R. Maddrell, Mater. Res. Soc. Symp. Proc. 1107 (2008) 413–420.
[19] M.C. Stennett, N.C. Hyatt, D.P. Reid, E.R. Maddrell, N. Peng, C. Jeynes, K.J. Kirkby, J.C. Woicik, Mater. Res. Soc. Symp. Proc. 1124 (2009) 243–248.
[20] N.C. Hyatt, M. Stennett, A. Jenni, D. Reid, E.R. Maddrell, Mater. Res. Soc. Symp. Proc. 1193 (2009) 61–66.
[21] W.J. Weber, A. Navrotsky, S. Stefanovsky, E.R. Vance, E. Vernaz, MRS Bull. 34 (2009) 46–53.
[22] A.V. Ochkin, S.V. Stefanosky, A.G. Plashkin, N.S. Mikhailenko, O.I. Kirjanova, Mater. Res. Soc. Symp. Proc. 824 (2004) 267–272.
[23] F. Jorion, X. Deschanels, T. Advocat, F. Desmouliere, J.N. Cachia, S. Peuget, D. Roudil, G. Leturcq, Nucl. Sci. Eng. 153 (2006) 262–271.
[24] G.R. Lumpkin, Elements 2 (2006) 365–372.
[25] D.M. Strachan, R.D. Scheele, E.C. Buck, A.E. Kozelisky, R.L. Sell, R.J. Elovich, W.C. Buchmiller, J. Nucl. Mater. 372 (2008) 6–31.
[26] A.E. Ringwood, S.E. Kesson, N.G. Ware, W.O. Hibberson, A. Major, Geochem. J. 13 (1979) 141–165.
[27] P.E. Fielding, T.J. White, J. Mater. Res. 2 (1987) 387–414.
[28] Y. Zhang, M.W.A. Stewart, H.Li;M.L. Carter, E.R. Vance, S. Moricca, J. Nucl. Mater. 395 (2009) 69–74.
[29] F. Farges, R.C. Ewing, G.E. Brown, J. Mater. Res. 8 (1993) 1983–1995.
[30] R.C. Ewing, W.J. Weber, W. Lutze, Disposal of weapon plutonium approaches and prospects, in: E.R. Merz, C.E. Walter (Eds.), Kluwer Dordrecht, The Netherlands, 1995, pp. 65–83.
[31] W.J. Weber, J.W. Wald, Hj. Matzke, J. Non-Cryst. Solids 138 (1986) 196–209.
[32] G.R. Lumpkin, R.C. Ewing, B.C. Chakoumakos, R.B. Greegor, F.W. Lytle, E.M. Foltyn, F.W. Clinard, L.A. Boatner, M.M. Abraham, J. Mater. Res. 1 (1986) 564–576.
[33] J.W. Wald, W.J. Weber, Advances in ceramics, nuclear waste management, vol. 8, in: G. Wicks, W.A. Ross (Eds.), American Ceramic Society, Columbus, OH, 1984, pp. 71–75.
[34] K. Smith, Z. Zhang, P. McGlinn, D. Attard, H. Li, G.R. Lumpkin, M. Colella, T. McLeod, Z. Aly, E. Loi, S. Leung, K.P. Hart, M. Ridway, W.J. Weber, S. Thevuthasan, Mater. Res. Soc. Symp. Proc. 757 (2003) 289–296.
[35] T. Wiss, X. Deschanels, J.P. Hiernaut, D. Roudil, S. Peuget, V.V. Rondinella, J. Nucl. Mater. 362 (2007) 431–437.
[36] H.J. Rossell, Nature 283 (1980) 282–283.
[37] B. Gatehouse, I.E. Gray, R.J. Hill, H.J. Rossell, Acta Cryst. B 37 (1981) 306–312.
[38] R.W. Cheary, A.A. Coelho, Phys. Chem. Miner. 24 (1997) 447–454.
[39] B.D. Begg, E.R. Vance, R.A. Day, M. Hambley, S.D. Conradson, Mater. Res. Soc. Symp. Proc. 465 (1997) 325–332.
[40] B.D. Begg, E.R. Vance, S.D. Conradson, J. Alloys Compd. 271–273 (1998) 221–226.
[41] B.D. Begg, R.A. Day, A. Brownscombe, Mater. Res. Soc. Symp. Proc. 663 (2001) 259–266.
[42] B.D. Begg, E.R. Vance, Mater. Res. Soc. Symp. Proc. 465 (1997) 333–340.
[43] E.R. Vance, R.A. Day, B.D. Begg, P.J. Angel, Int. Ceram. Monogr. 1 (1994) 1301–1306.
[44] S.V. Stefanovky, A.Y. Troole, M.I. Lapina, B.S. Nikonov, A.V. Sivtsov, S.V. Yudintsev, Mater. Res. Soc. Symp. Proc. 713 (2002) 345–350.
[45] X. Deschanels, V. Picot, B. Glorieux, F. Jorion, S. Peuget, D. Roudil, C. Jégou, V. Broudic, J.N. Cachia, T. Advocat, C. Den Auwer, C. Fillet, J.P. Coutures, C. Hennig, A. Scheinost, J. Nucl. Mater. 352 (2006) 233–240.
[46] R.D. Shannon, Acta Cryst. A 32 (1976) 751–767.
[47] E.R. Vance, A. Jostsons, R.A. Day, C.J. Ball, B.D. Begg, P.J. Angel, Mater. Res. Soc. Symp. Proc. 412 (1996) 41–47.
[48] P. Loiseau, D. Caurant, N. Baffier, C. Fillet, Mater. Res. Soc. Symp. Proc. 757 (2003) 243–250.
[49] E.R. Vance, C.J. Ball, R.A. Day, K.L. Smith, M.G. Blackford, B.D. Begg, P.J. Angel, J. Alloys Compd. 213–214 (1994) 406–409.
[50] G.R. Lumpkin, K.R. Whittle, C.J. Howard, Z. Zhang, F.J. Berry, G. Oates, C.T. Williams, A.N. Zaitsev, Mater. Res. Soc. Symp. Proc. 932 (2006) 639–645.
[51] P. Loiseau, D. Caurant, O. Majérus, N. Baffier, C. Fillet, J. Mater. Sci. 38 (2003) 843–852.
[52] P. Loiseau, D. Caurant, N. Baffier, C. Fillet, Mater. Res. Soc. Symp. Proc. 663 (2001) 169–177.
[53] P. Loiseau, D. Caurant, N. Baffier, L. Mazerolles, C. Fillet, Mater. Res. Soc. Symp. Proc. 663 (2001) 179–187.
[54] P. Loiseau, D. Caurant, N. Baffier, C. Fillet, Phys. Chem. Glasses 43C (2002) 201–206.
[55] P. Loiseau, D. Caurant, O. Majérus, N. Baffier, L. Mazerolles, C. Fillet, Phys. Chem. Glasses 43C (2002) 195–200.
[56] P. Loiseau, D. Caurant, N. Baffier, L. Mazerolles, C. Fillet, J. Nucl. Mater. 402 (2010) 38–54.
[57] M. Mahmoudysepehr, V.K. Marghussian, J. Am. Ceram. Soc. 92 (2009) 1540–1546.
[58] E. Balan, D.R. Neuville, P. Trocellier, E. Fritsch, J-P. Muller, G. Calas, Am. Mineral. 86 (2001) 1025–1033.
[59] B.E. Burakov, E.B. Anderson, M.V. Zamoryanskaya, M.A. Yagovkina, E.E. Strykanova, E.V. Nikolaeva, Mater. Res. Soc. Symp. Proc. 663 (2001) 307–313.
[60] W.L. Gong, W. Lutze, R.C. Ewing, J. Nucl. Mater. 277 (2000) 239–249.
[61] R. Giéré, C.T. Williams, G. R Lumpkin, Schweiz. Mineral. Petrogr. Mitt. 78 (1998) 433–459.
[62] R.A. McCauley, F.A. Hummel, J. Solid State Chem. 33 (1980) 99–105.
[63] D. Swenson, T.G. Nieh, J.H. Fournelle, Mater. Res. Soc. Symp. Proc. 412 (1996) 337–344.
[64] R.L. Putnam, A. Navrotsky, B.F. Woodfield, J.L. Shapiro, R. Stevens, J. Boerio-Goates, Mater. Res. Soc. Symp. Proc. 556 (1999) 11–18.
[65] J. Emsley, The Elements, Clarendon Press (Ed.), Oxford, 1992.
[66] D.S. Perera, M.W.A. Stewart, H. Li, R.A. Day, E.R. Vance, J. Am. Ceram. Soc. 85 (2002) 2919–2924.
[67] H.J. Rossell, J. Solid State Chem. 99 (1992) 38–51.
[68] K.P. Hart, E.R. Vance, M.W. Stewart, J. Weir, M.L. Carter, M. Hambley, A. Brownscombe, R.A. Day, S. Leung, C.J. Ball, B. Ebbinghaus, L. Gray, T. Kan, Mater. Res. Soc. Symp. Proc. 506 (1998) 161–168.
[69] R. Giéré, J. Malmström, E. Reusser, G.R. Lumpkin, M. Düggelin, D. Mathys, R. Guggenheim, D. Günther, Mater. Res. Soc. Symp. Proc. 663 (2001) 267–275.
[70] G.R. Lumpkin, K.R. Whittle, S. Rios, K.L. Smith, N.J. Zaluzec, J. Phys.: Condens. Matter 16 (2004) 8557–8570.
[71] K.R. Whittle, M.G. Blackford, G.R. Lumpkin, K.L. Smith, N.J. Zaluzec, Mater. Res. Soc. Symp. Proc. 1124 (2009) 237–242.
[72] P. Loiseau, D. Caurant, I. Bardez, O. Majérus, N. Baffier, C. Fillet, Mater. Res. Soc. Symp. Proc. 757 (2003) 281–287.
[73] D. Caurant, I. Bardez, P. Loiseau, J. Mater. Sci. 42 (2007) 10203–10218.
[74] P. Loiseau, Contribution to the study of zirconolite ($CaZrTi_2O_7$) based glass–ceramics and ceramics devoted to the immobilization of long-lived radionuclides, PhD. Thesis, University Paris 6, France, 2001.
[75] D. Caurant, P. Loiseau, I. Bardez, C. Gervais, J. Mater. Sci. 42 (2007) 8558–8570.
[76] J. Rodriguez-Carjaval, in Abstracts of the Satellite Meetings on Powder Diffraction of the XV Congress of the IUCr, Toulouse, France, 1990, p. 127.
[77] V. Metha, D. Gourier, A. Mansingh, A.L. Dawar, Solid State Commun. 109 (1999) 513–517.
[78] N.P. Laverov, S.V. Yudinstev, M.I. Lapina, S.V. Stefanovsky, S.C. Chae, R.C. Ewing, Mater. Res. Soc. Symp. Proc. 757 (2003) 321–328.
[79] R.W. Cheary, J. Solid State Chem. 98 (1992) 323–329.
[80] G.R. Lumpkin, K.L. Smith, M.G. Blackford, J. Nucl. Mater. 224 (1995) 31–42.
[81] T. Kushida, Phys. Rev. 185 (1969) 500–508.